Published in "Nature doi: 10.1038/nature10873, 2012"
which should be cited to refer to this work.

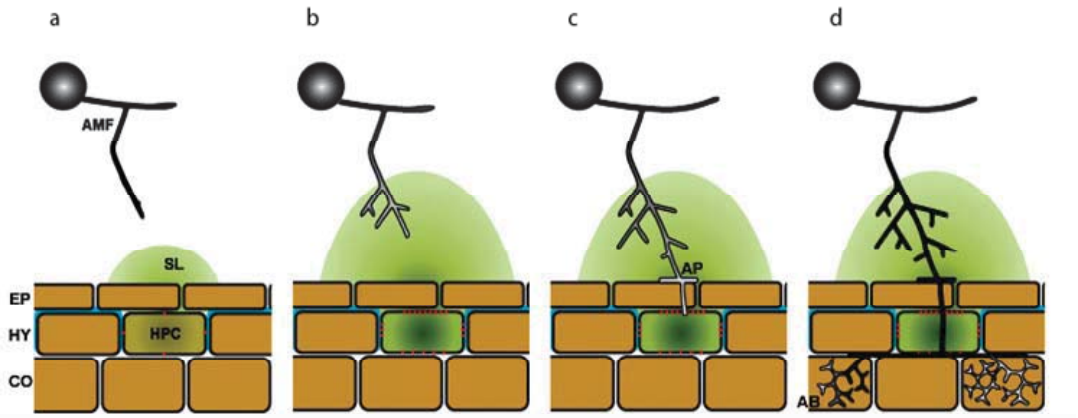

Supplementary figure 1 | Model for PDR1-dependent strigolactone (SL) exudation from hypodermal passage cells (HPC) and its effect on arbuscular mycorrhizal fungi (AMF)
Colonization rates of AMF reciprocally correlate with the phosphate status of the plant and it was suggested that differential exudation of SLs are partly responsible[1]. SL exudation has been demonstrated to be enhanced under low phosphate availability, when the plant benefits most from the symbiosis with AMF[2]. Extraradical AMF hyphal proliferation depends on SL perception within the rhizosphere that signals the vicinity of a susceptible mycotrophic root[3]. In absence of SLs AMF remain dormant and interaction is less likely to occur. Situated below the epidermis (EP), the hypodermis (HY) defines the outer boundary of the root cortex (CO). In plant species with a dimorphic hypodermis, hypodermal passage cells constitute single un-suberized cells in a matrix of suberized (blue layer) hypodermal cells[4]. In order to reach the cortex, where arbuscle formation and nutrient exchange takes place, AMF exclusively pass through HPCs[5].
a, Under phosphate sufficient conditions, SL production is low, which, in concomitance with low *PDR1* expression (red ellipses = PDR1), results in levels of SL exudation (green gradient) from HPCs that are not sufficient to activate AMF hyphal metabolism.
b, Under phosphate deficient conditions SL biosynthesis and *PDR1* expression are up-regulated, resulting in increased SL exudation from HPCs. AMF metabolism is activated and vigorous hyphal branching and proliferation is induced.
c, Guided by the SL gradient, AMF encounter the root surface, form appressoria (AP) in the proximity of HPCs and penetrate the epidermal layer.
d, After successful cortical entry via penetration of HPCs, AMF can expand laterally and intracellularly within the cortex and form symbiotic structures such as arbuscles (AB).

References:

1. Balzergue, C., Puech-Pagès, V., Bécard, G. & Rochange, S. F. The regulation of arbuscular mycorrhizal symbiosis by phosphate in pea involves early and systemic signalling events. *Journal of Experimental Botany* **62(3)**, 1049-1060 (2011)
2. Lopez-Raez, J. A. et al. Tomato strigolactones are derived from carotenoids and their biosynthesis is promoted by phosphate starvation. *New Phytol* **178**, 863-874 (2008).
3. Akiyama, K., Matsuzaki, K.-i. & Hayashi, H. Plant sesquiterpenes induce hyphal branching in arbuscular mycorrhizal fungi. *Nature* **435**, 824-827 (2005).
4. Enstone, D., Peterson, C. & Ma, F. in *Journal of Plant Growth Regulation* 335-351 (Springer New York, 2003).
5. Sharda, J. N. & Koide, R. T. Can hypodermal passage cell distribution limit root penetration by mycorrhizal fungi? *New Phytologist* **180**, 696-701 (2008).

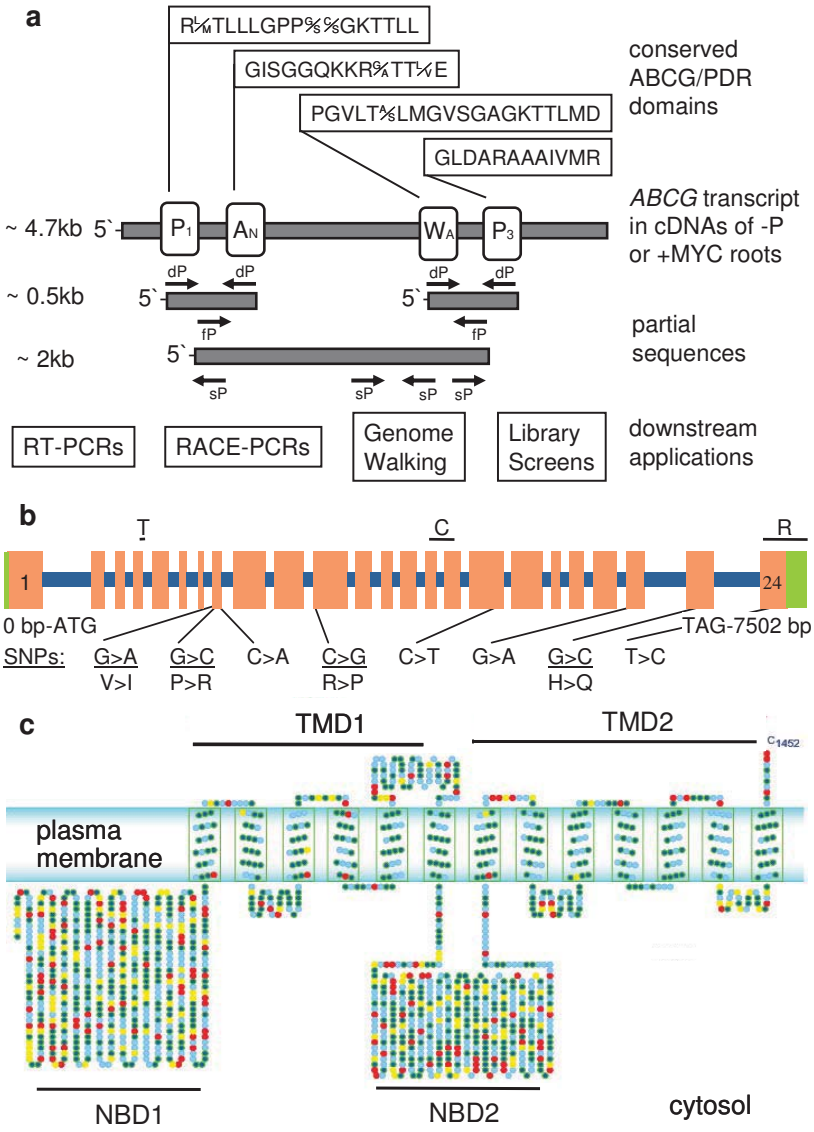

Supplementary figure 2 | Screening approach to identify *ABCG/PDR* candidate genes, genomic structure of *PDR1* and predicted protein topology of PDR1

a, Degenerate primer approach for amplification of ABCG/PDR candidate sequences from the cDNA of phosphate starved (-P) or 8 wpi *G. intraradices*-colonized (+MYC) roots of W115. Conserved ABCG/PDR domains[1]: P1 = PDR signature1, AN = N-terminal ABC signature, WA = Walker A motif, P3 = PDR signature 3. dP = degenerate primer, fP = subfamily specific primer, sP = sequence specific primer, **b**, Predicted genomic structure of *P. hybrida PDR1* and its *P. axillaris* orthologue *PaPDR1* (JQ292812), depicting exons (orange), introns (blue) and UTRs (green). SNPs shows 8 single nucleotide polymorphisms (SNPs) found between the coding regions of *PhPDR1* (JQ292813) and *PaPDR1* (*PhPDR1*>*PaPDR1*). Non-synonymous SNPs are underlined and the corresponding 4 amino acid changes are indicated below. All 4 conversions are found in variable PDR protein regions[1]. T indicates *dTph1* insertion site in *PhPDR1*. C and R indicate *PDR1*-specific target regions of RNAi constructs. *PDR1* RT primers were specific for C or R region. **c,** Putative transmembrane topology of PDR1 (1452 amino acids), featuring a PDR-specific reverse orientation with an initial cytosolic nucleotide binding domain (NBD1) followed by a transmembrane domain (TMD1). TMD1 is followed by NBD2 and TMD2. Hydrophobic (green circles), hydrophilic (blue circles), positively charged (red circles) and negatively charged (yellow circles) residues are depicted.

References:

1. van den Brule, S. & Smart, C. C. The plant PDR family of ABC transporters. *Planta* **216**, 95-9106 (2002).

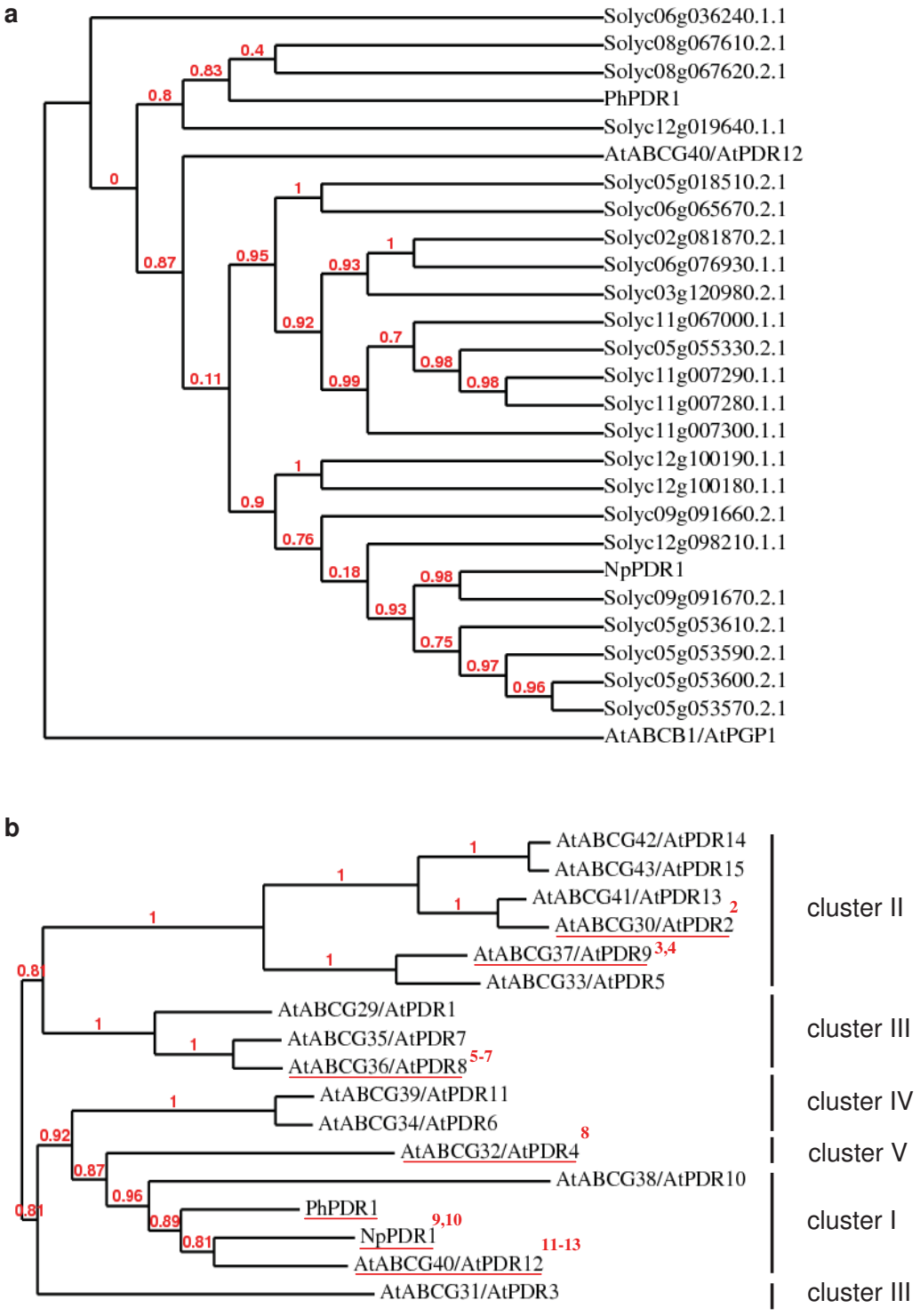

Supplementary figure 3 | Predicted ABCG/PDR family of *Solanum lycopersicum* (tomato) and phylogenetic position of *P. hybrida* PDR1 in relation to the Arabidopsis full size ABCG/PDR subfamily of ABC transporters

a, Maximum likelihood-based phylogenetic tree for putative Solanum lycopersicum full-size ABCG/PDR proteins based on a BLAST search on the http://mips.helmholtz-muenchen.de/plant/tomato/ database. The ABCG members AtABCG40/AtPDR12 (BK001011), NpPDR1 (CAC40990) and PhPDR1 (JQ292813) are included. The *Arabidopsis* auxin transporter AtABCB1/AtPGP1 (Q9ZR72) was used to root the tree. Numbers in red at branches indicate

nonparametric bootstrap values. **b**, Maximum likelihood-based phylogenetic position of PhPDR1 in relation to the Arabidopsis full-size ABCG/PDR subfamily of ABC transporters and NpPDR1. Numbers in red at branches indicate nonparametric bootstrap values. PDR-specific clusters are indicated as previously defined[1]. Proteins underlined in red have been characterized on a functional level[2-13]. Accessions: AtPDR1 (BK001001), AtPDR2 (BK001000), AtPDR3 (BK001002), AtPDR4 (BK001003), AtPDR5 (BK001004), AtPDR6 (BK001005), AtPDR7 (BK001006), AtPDR8 (BK001007), AtPDR9 (BK001008), AtPDR10 (BK001009), AtPDR11 (BK001010), AtPDR12 (BK001011), AtPDR13 (BK001012), AtPDR14 (BK001013), AtPDR15 (BK001014), NpPDR1 (CAC40990), PhPDR1 (JQ292813)

References:

1. Crouzet, J., Trombik, T., Fraysse, A. S. & Boutry, M. Organization and function of the plant pleiotropic drug resistance ABC transporter family. *FEBS Lett* **580**, 1123-1130 (2006).
2. Badri, D. V. et al. An ABC transporter mutation alters root exudation of phytochemicals that provoke an overhaul of natural soil microbiota. *Plant Physiol* **151**, 2006-2017 (2009).
3. Ito, H. & Gray, W. M. A gain-of-function mutation in the Arabidopsis pleiotropic drug resistance transporter PDR9 confers resistance to auxinic herbicides. *Plant Physiol* **142**, 63-74 (2006).
4. Ruzicka, K. et al. Arabidopsis PIS1 encodes the ABCG37 transporter of auxinic compounds including the auxin precursor indole-3-butyric acid. *Proc Natl Acad Sci U S A* **107**, 10749-10753 (2010).
5. Kobae, Y. et al. Loss of AtPDR8, a plasma membrane ABC transporter of Arabidopsis thaliana, causes hypersensitive cell death upon pathogen infection. *Plant Cell Physiol* **47**, 309-318 (2006).
6. Stein, M. et al. Arabidopsis PEN3/PDR8, an ATP binding cassette transporter, contributes to nonhost resistance to inappropriate pathogens that enter by direct penetration. *Plant Cell* **18**, 731-746 (2006).
7. Kim, D.-Y., Bovet, L., Maeshima, M., Martinoia, E. & Lee, Y. The ABC transporter AtPDR8 is a cadmium extrusion pump conferring heavy metal resistance. *Plant J* **50**, 207-218 (2007).
8. Bessire, M. et al. A Member of the PLEIOTROPIC DRUG RESISTANCE Family of ATP Binding Cassette Transporters Is Required for the Formation of a Functional Cuticle in Arabidopsis *The Plant Cell Online* **23** 1958-1970 (2011).
9. Jasinski, M. et al. A plant plasma membrane ATP binding cassette-type transporter is involved in antifungal terpenoid secretion. *Plant Cell* **13**, 1095-1107 (2001).
10. Stukkens, Y. et al. NpPDR1, a pleiotropic drug resistance-type ATP-binding cassette transporter from Nicotiana plumbaginifolia, plays a major role in plant pathogen defense. *Plant Physiol* **139**, 341-352 (2005).
11. Campbell, E. J. et al. Pathogen-responsive expression of a putative ATP-binding cassette transporter gene conferring resistance to the diterpenoid sclareol is regulated by multiple defense signaling pathways in Arabidopsis. *Plant Physiol* **133**, 1272-1284 (2003).
12. Lee, M., Lee, K., Lee, J., Noh, E. W. & Lee, Y. AtPDR12 contributes to lead resistance in Arabidopsis. *Plant Physiol* **138**, 827-836 (2005).
13. Kang, J. et al. PDR-type ABC transporter mediates cellular uptake of the phytohormone abscisic acid. *Proc Natl Acad Sci U S A* **107**, 2355-2360 (2010).

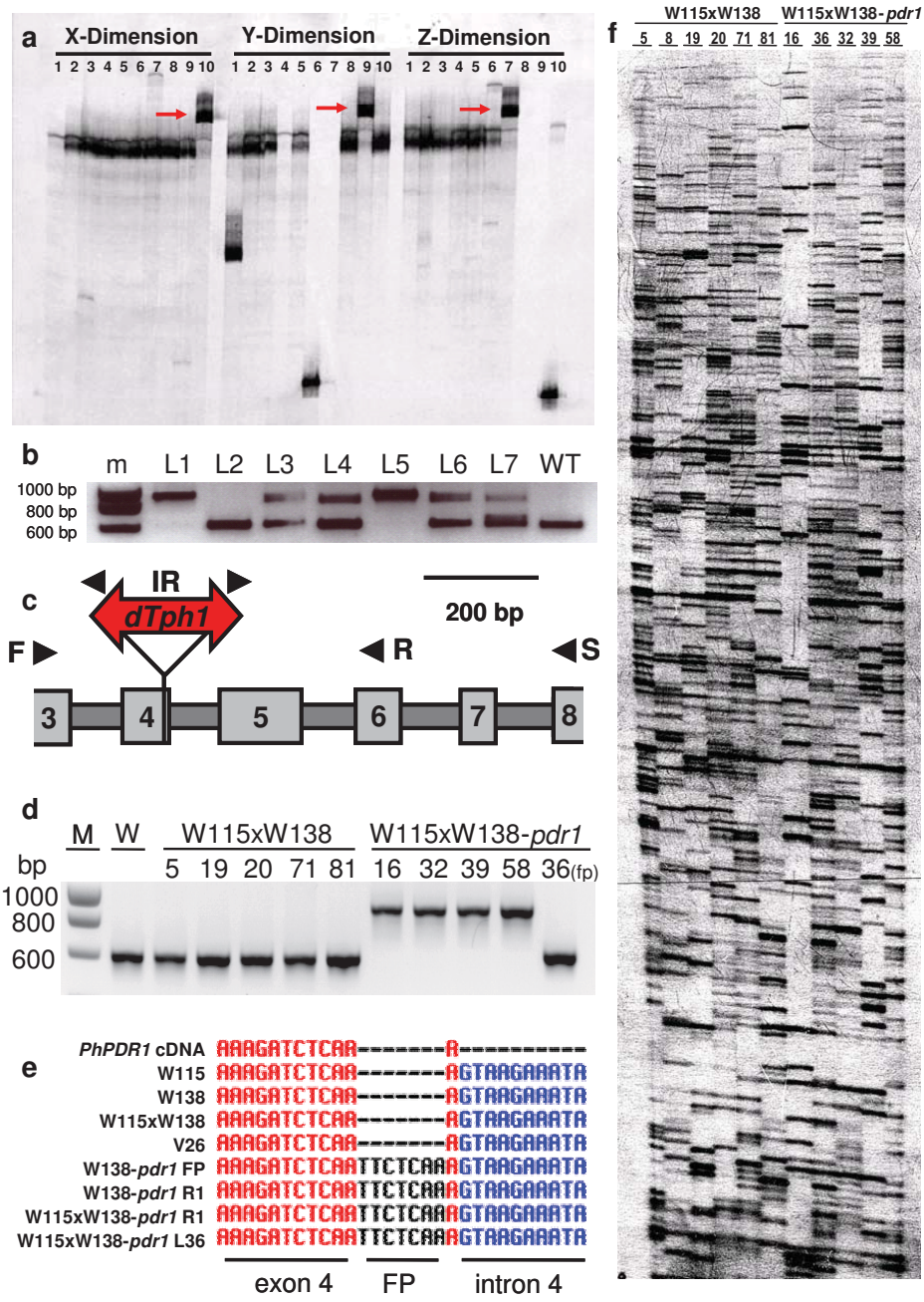

Supplementary figure 4 | Genetic analysis of a *dTph1* insertion in *PDR1* in the *P. hybrida* W138 and the W115xW138 background

a, PCR-based screen of a three dimensionally arranged gDNA library of 10x10x10 W138 individuals for *dTph1* insertion in *PDR1*. Amplification with a *dTph1*-specific primer (IR in **c**) and a *PDR1*-specific primer (S in **c**) resulted in one specific band per dimension (red arrows), giving coordinates for a single W138 individual (X-10, Y-9, Z-7). **b,** Homozygosity PCR with transposon flanking primers identifying homozygous *PDR1 dTph1* insertion mutants (L1 and L5), heterozygous individuals (L3, L4, L6, and L7) and a putative homozygous *PDR1* wild-type (L2) in the selfed progeny of the retrieved candidate. W115 (WT) served as a wild-type control (m, marker lane). Sequencing of L2 revealed homozygosity for a 7 bp target site duplication-derived footprint allele (W138-*pdr1* FP in **e**). **c,** Schematic of *dTph1* insertion in exon 4 of *PDR1*. Black triangles indicate positions of primers used in the screen (IR and S) and for homozygosity PCR (F and R). **d,** Homozygosity PCR for *dTph1* insertion on the selfed progeny of W115 crosses with W138-*pdr1* (primers F and R in **b**). M corresponds to marker lane and W115 (W) served as control. Five lanes correspond to homozygous *PDR1* wild-type lines (W115xW138), four lanes correspond to

homozygous *PDR1 dTph1* insertion lines (W115xW138-*pdr1*) and one lane corresponds to a homozygous *PDR1* footprint allele (36 (fp)). **e,** Alignment of the footprint flanking region of W115 cDNA with *PDR1* wild-type and *PDR1* footprint alleles in various *P. hybrida* backgrounds. (FP = footprint, R = somatic revertant). **f,** Transposon display of *dTph1* insertions in the background of six W115xW138 and five W115xW138-*pdr1* lines. Line 8 was not used for phenotypic analysis in this study. Bands that co-segregate strictly with the presence or absence of the *PDR1 dTph1* insertion or the respective phenotypes indicate *dTph1* insertions that could also be responsible for the observed phenotypes. Note that the *dTph1* insertion in *PDR1* cannot be detected on this display due to an expected band size of 1.7 kb that is beyond the resolution of the display.

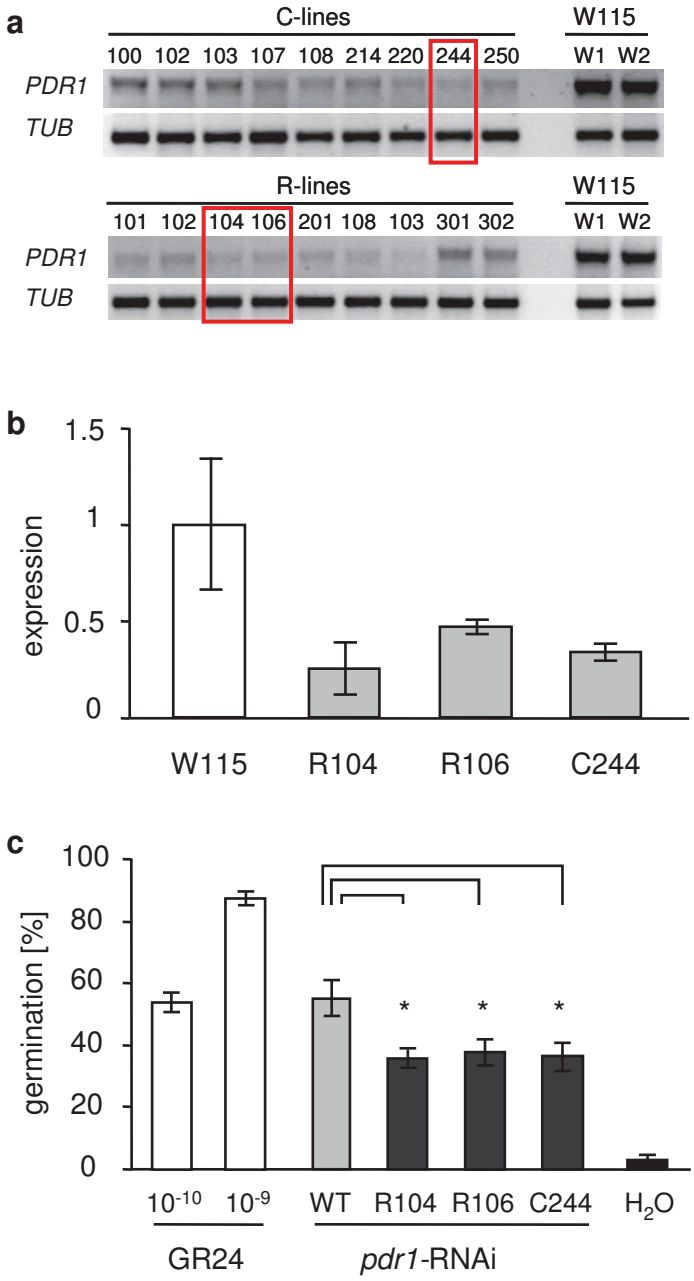

Supplementary figure 5 | *PDR1* transcript quantification and assessment of stimulation of germination of *P. ramosa* for *pdr1*-RNAi lines

a, Semiquantitative RT-PCR for *PDR1* transcript in seedlings of W115 lines either transformed with a silencing construct targeting a non-conserved region in the center of *PDR1* (C-lines) or the 3`end and 3`untranslated region of *PDR1* (R-lines). Two untransformed W115 individuals (W1 and W2) served as wild-type controls and tubulin (*TUB*) served as loading control. Red boxes indicate lines used in this study. **b**, qRT PCR targeting *PDR1* transcript in W115 seedlings and selected RNAi lines. Data was normalized against *Glyceraldehyde 3-phosphate dehydrogenase* and W115 *PDR1* expresssion. Data are means ± s.e.m. (N = 3). **c**, Germination of *P. ramosa* induced by root exudates from W115 and three independent *pdr1*-RNAi lines (N = 4). GR24 at 1 and 0.1 nM served as positive control and water (H2O) served as negative control (N = 3). Data are means ± s.e.m. * = $p<0.05$

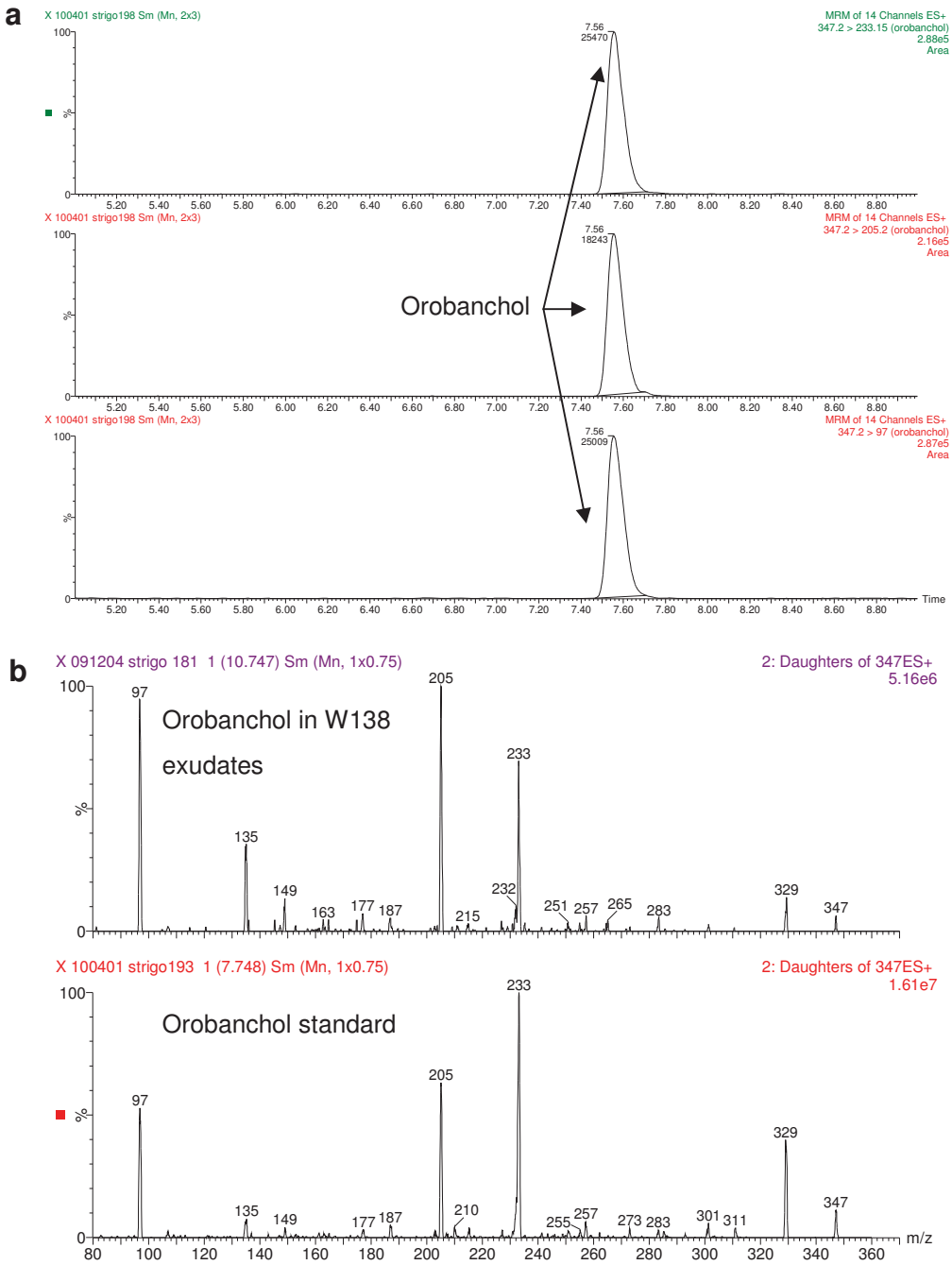

Supplementary figure 6 | Orobanchol identification in *P. hybrida*
a, MRM-LC-MS/MS chromatogram of W138 exudates showing transitions 347 > 233, 347 > 205 and 347 > 96.8, for orobanchol. **b**, full daughter ion scan MS/MS spectrum of orobanchol in W138 exudates and orobanchol standard.

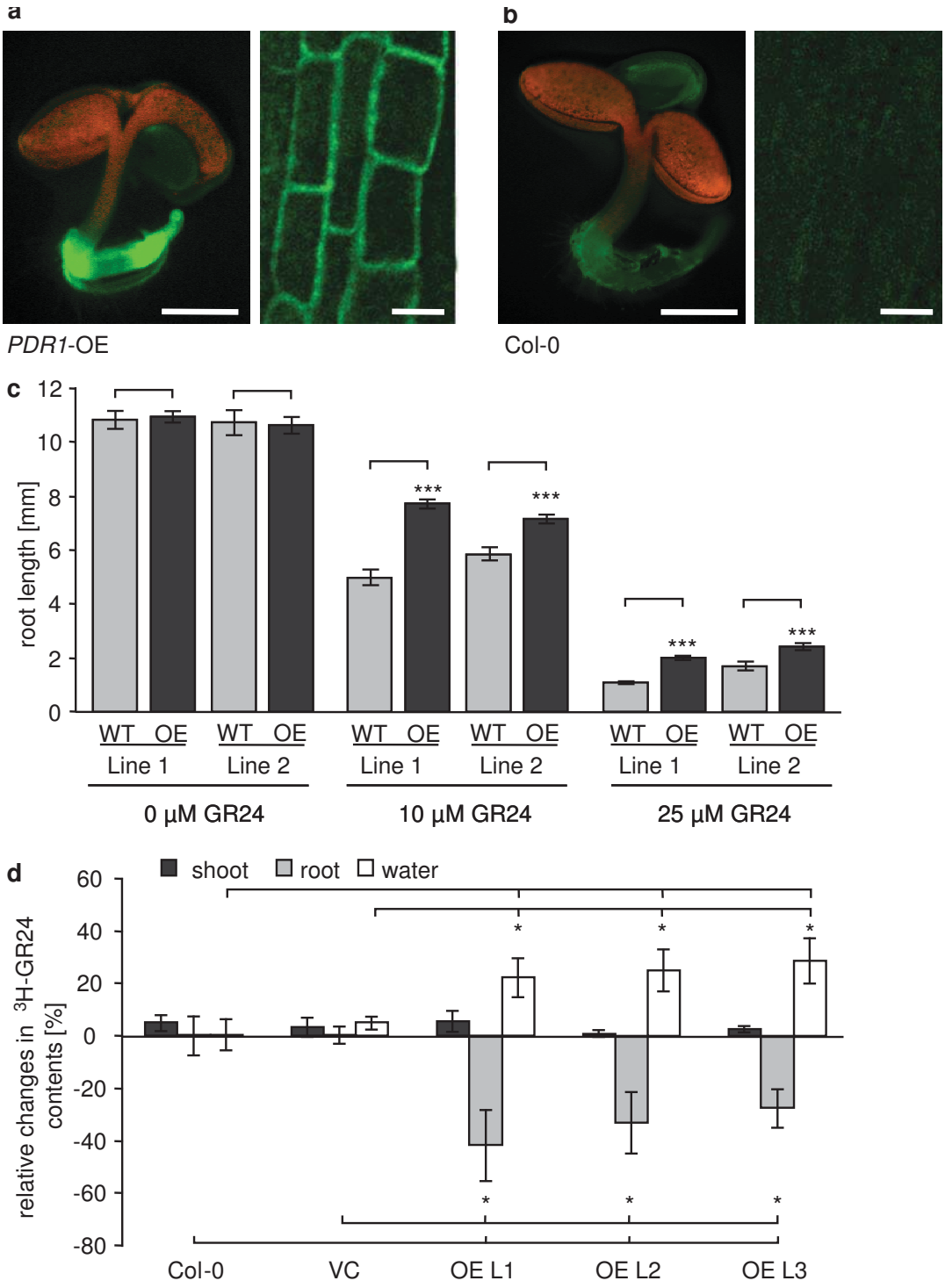

Supplementary figure 7 | Evaluation of *PDR1*-OE lines
a-b, GFP signal in whole seedlings (left panels, Scale bar = 1 mm) and epidermal root cells (right panels, Scale bar = 10 µm) of a *GFP::gPaPDR1* overexpression line (*PDR1*-OE) (**a**) and autofluorescence in Col-0 (**b**). **c**, Quantification of root length of two independent *PDR1*-OE lines (dark grey) (N > 36) and segregating wild-types (grey) (N > 12) germinated and grown for 7 days on 0, 10 or 25 µM GR24. *** = $p < 0.001$. **d,** Transport-related changes in GR24 contents in shoots, roots and root exudates. GR24 contents of metabolically inactive tissues incubated for 1 h at 4°C were subtracted from contents of metabolically active tissues incubated for 1 h at 23°C. The differences are displayed in percent analogous to the graph in Fig. 3d. * = $p < 0.05$. OE L1-OE L3 are three independent *PDR1*-OE lines

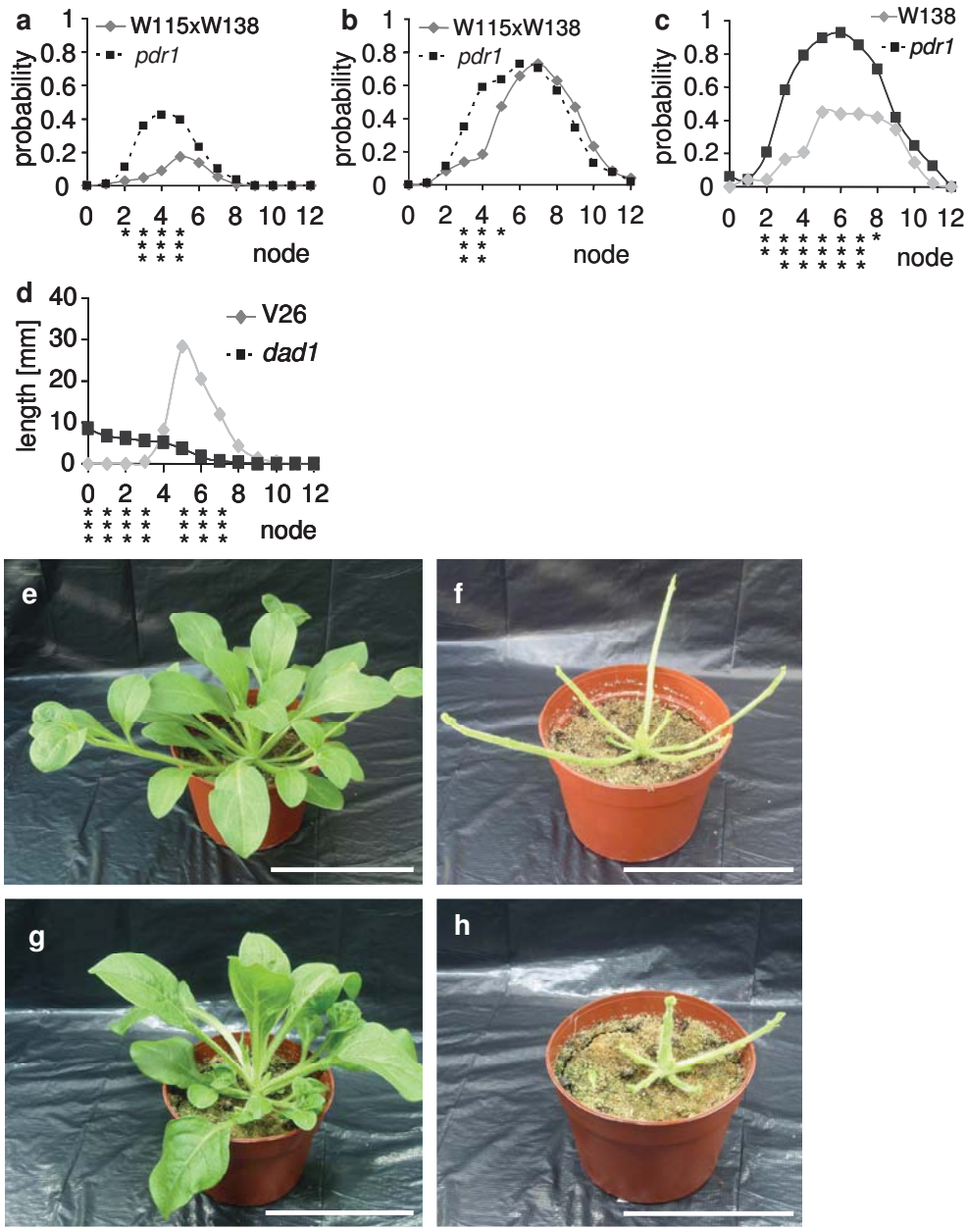

Supplementary figure 8 | Aboveground phenotype of *pdr1* and *dad1* lines
a-b Analysis of branch development of W115xW138 (grey diamonds) and W115xW138-*pdr1* (black squares). Probability at a given node to produce a bud of more than 7 mm 29 dpg (**a**) and a fully developed branch at flowering time 55 dpg (**b**). Data are means ± s.e.m. (N = 110 (5x22)). **c**, Probability at a given node to produce a fully developed branch for W138 and W138-*pdr1* at flowering time 64 dpg. Data are means ± s.e.m. (N = 49). Note: The comparably stronger branching phenotype of W138-*pdr1* over W115xW138-*pdr1* is attributed to the transposon backgrounds of W138 that are assumed to cause pleiotropic aboveground effects. These result in a relatively weaker branching performance of W138 and stronger response to lack of *PDR1*-dependent SL distribution in W138-*pdr1*. These effects are largely compensated in the W115xW138 crosses, which show a near identical branching phenotype as the *pdr1*-RNAi lines (Fig. 4e-f; Supplementary table 1). We believe that W115xW138 crosses and *pdr1*-RNAi reflect the aboveground effects of *PDR1* impairments more adequately. As opposed to the complex trait of branching, SL exudation is dominantly PDR1-controlled, causing similar effects in all *pdr1* backgrounds. **d**, Branch length at a given node for V26 and *dad1* 35 dpg Data are means ± s.e.m. (N = 8) **e-h**, Visible branch length phenotype 41 dpg of a W115xW138-*pdr1* individual (**e**), stripped of its leaves (**f**) as compared to a W115xW138 individual (**g**), stripped of its leaves (**h**). Scale bars = 10 cm.

	WT	*pdr1*	*pdr1*/ WT	P-value	dpg
W138	2.7 +/ - 0.28	5.9 +/ - 0.24	2.19	>0.001 (n=49)	64
W115xW138	3.8 +/ - 0.02	4.3 +/ - 0.02	1.13	>0.001 (n=110)	58
W115 (RNAi)	3.6 +/ - 0.37	4.2 +/ - 0.38	1.17	n.s. (n=15)	58
	WT	*dad1*	*dad1*/ WT		
V26	3.4 +/ - 0.48*	9.9 +/ - 0.99*	2.91	>0.001 (n=7)*	70

Supplementary table 1 | Number of branches at flowering time in *pdr1* and *dad1* lines
Total number of full branches of *pdr1* mutants and the respective wild-types at flowering time were scored according to a petunia branch definition[1]. For comparison full branch numbers of V26 and *dad1* as presented by Napoli[2] (*) are shown. dpg = days post germination; Note: The comparably stronger pdr1/WT ratio of W138-*pdr1* over W115xW138-*pdr1* is attributed to the transposon backgrounds of W138 that are assumed to cause pleiotropic aboveground effects. These result in a lower branch number of W138 and stronger response to lack of *PDR1*-dependent SL distribution in W138-*pdr1*. These effects are largely compensated in the W115xW138 crosses, which show a near identical branching phenotype as the *pdr1*-RNAi lines (Fig. 4e-f). We believe that W115xW138 crosses and *pdr1*-RNAi reflect the aboveground effects of *PDR1* impairments more adequately.

References:

1. Snowden, K. C. & Napoli, C. A. A quantitative study of lateral branching in petunia. *Functional Plant Biology* **30**, 987-994 (2003).
2. Napoli, C. Highly Branched Phenotype of the Petunia dad1-1 Mutant Is Reversed by Grafting. *Plant Physiol* **111**, 27-37 (1996).